Deep exclusive electroproduction of π^0 at high Q^2 in the quark valence regime

M. Dlamini,[1] B. Karki,[1] S.F. Ali,[2] P-J. Lin,[3] F. Georges,[3] H-S Ko,[3,4] N. Israel,[1] M.N.H. Rashad,[5] A. Stefanko,[6] D. Adikaram,[7] Z. Ahmed,[8] H. Albataineh,[9] B. Aljawrneh,[10] K. Allada,[11] S. Allison,[5] S. Alsalmi,[12] D. Androic,[13] K. Aniol,[14] J. Annand,[15] H. Atac,[16] T. Averett,[17] C. Ayerbe Gayoso,[17] X. Bai,[18] J. Bane,[19] S. Barcus,[17] K. Bartlett,[17] V. Bellini,[20] R. Beminiwattha,[21] J. Bericic,[7] D. Biswas,[22] E. Brash,[23] D. Bulumulla,[5] J. Campbell,[24] A. Camsonne,[7] M. Carmignotto,[2] J. Castellano,[25] C. Chen,[22] J-P. Chen,[7] T. Chetry,[1] M.E. Christy,[22] E. Cisbani,[26] B. Clary,[27] E. Cohen,[28] N. Compton,[1] J.C. Cornejo,[17,6] S. Covrig Dusa,[7] B. Crowe,[29] S. Danagoulian,[10] T. Danley,[1] F. De Persio,[26] W. Deconinck,[17] M. Defurne,[30] C. Desnault,[3] D. Di,[18] M. Duer,[28] B. Duran,[16] R. Ent,[7] C. Fanelli,[11] G. Franklin,[6] E. Fuchey,[27] C. Gal,[18] D. Gaskell,[7] T. Gautam,[22] O. Glamazdin,[31] K. Gnanvo,[18] V.M. Gray,[17] C. Gu,[18] T. Hague,[12] G. Hamad,[1] D. Hamilton,[15] K. Hamilton,[15] O. Hansen,[7] F. Hauenstein,[5] W. Henry,[16] D.W. Higinbotham,[7] T. Holmstrom,[32] T. Horn,[2,7] Y. Huang,[18] G.M. Huber,[8] C. Hyde,[5] H. Ibrahim,[33] C-M. Jen,[34] K. Jin,[18] M. Jones,[7] A. Kabir,[12] C. Keppel,[7] V. Khachatryan,[7,35,36] P.M. King,[1] S. Li,[37] W. Li,[8] J. Liu,[18] H. Liu,[38] A. Liyanage,[22] J. Magee,[17] S. Malace,[7] J. Mammei,[39] P. Markowitz,[25] E. McClellan,[7] F. Meddi,[26] D. Meekins,[7] K. Mesik,[40] R. Michaels,[7] A. Mkrtchyan,[2] R. Montgomery,[15] C. Muñoz Camacho,[3] L.S. Myers,[7] P. Nadel-Turonski,[7] S.J. Nazeer,[22] V. Nelyubin,[18] D. Nguyen,[18] N. Nuruzzaman,[22] M. Nycz,[12] O.F. Obretch,[27] L. Ou,[11] C. Palatchi,[18] B. Pandey,[22] S. Park,[35] K. Park,[5] C. Peng,[41] R. Pomatsalyuk,[31] E. Pooser,[7] A.J.R. Puckett,[27] V. Punjabi,[42] B. Quinn,[6] S. Rahman,[39] P.E. Reimer,[43] J. Roche,[1,*] I. Sapkota,[2] A. Sarty,[44] B. Sawatzky,[7] N.H. Saylor,[45] B. Schmookler,[11] M.H. Shabestari,[46] A. Shahinyan,[47] S. Sirca,[48] G.R. Smith,[7] S. Sooriyaarachchilage,[22] N. Sparveris,[16] R. Spies,[39] T. Su,[12] A. Subedi,[46] V. Sulkosky,[11] A. Sun,[6] L. Thorne,[6] Y. Tian,[49] N. Ton,[18] F. Tortorici,[20] R. Trotta,[50] G.M. Urciuoli,[26] E. Voutier,[3] B. Waidyawansa,[7] Y. Wang,[17] B. Wojtsekhowski,[7] S. Wood,[7] X. Yan,[51] L. Ye,[46] Z. Ye,[18] C. Yero,[25] J. Zhang,[18] Y. Zhao,[35] and P. Zhu[52]

(The Jefferson Lab Hall A Collaboration)

[1] *Ohio University, Athens, Ohio 45701, USA*
[2] *Catholic University of America, Washington, DC 20064, USA*
[3] *Université Paris-Saclay, CNRS/IN2P3, IJCLab, 91405 Orsay, France*
[4] *Seoul National University, 1 Gwanak-ro, Gwanak-gu, 08826 Seoul, Korea*
[5] *Old Dominion University, Norfolk, Virginia 23529, USA*
[6] *Carnegie Mellon University, Pittsburgh, Pennsylvania 15213, USA*
[7] *Thomas Jefferson National Accelerator Facility, Newport News, Virginia 23606, USA*
[8] *University of Regina, Regina, SK, S4S 0A2 Canada*
[9] *Texas A&M University, Kingsville, Texas 77843, USA*
[10] *North Carolina Ag. and Tech. St. Univ., Greensboro, North Carolina 27411, USA*
[11] *Massachusetts Institute of Technology, Cambridge, Massachusetts 02139, USA*
[12] *Kent State University, Kent, Ohio 44240, USA*
[13] *University of Zagreb, Trg Republike Hrvatske 14, 10000, Zagreb, Croatia*
[14] *California State University, Los Angeles, Los Angeles, California 90032, USA*
[15] *SUPA School of Physics and Astronomy, University of Glasgow, Glasgow G12 8QQ, UK*
[16] *Temple University, Philadelphia, Pennsylvania 19122, USA*
[17] *The College of William and Mary, Williamsburg, Virginia 23185, USA*
[18] *University of Virginia, Charlottesville, Virginia 22904, USA*
[19] *University of Tennessee, Knoxville, Tennessee 37996, USA*
[20] *Istituto Nazionale di Fisica Nucleare, Dipt. Di Fisica delle Uni. di Catania, I-95123 Catania, Italy*
[21] *Syracuse University, Syracuse, NY 13244, USA*
[22] *Hampton University, Hampton, Virginia 23669, USA*
[23] *Christopher Newport University, Newport News, Virginia 23606, USA*
[24] *Dalhousie University, Nova Scotia, NS B3H 4R2, Canada*
[25] *Florida International University, Miami, Florida 33199, USA*
[26] *Istituto Nazionale di Fisica Nucleare - Sezione di Roma, P.le Aldo Moro, 2 - 00185 Roma, Italy*
[27] *University of Connecticut, Storrs, Connecticut 06269, USA*
[28] *Tel Aviv University, Tel Aviv-Yafo, Israel*
[29] *North Carolina Central University, Durham, North Carolina 27707, USA*
[30] *CEA Saclay, 91191 Gif-sur-Yvette, France*
[31] *Kharkov Institute of Physics and Technology, Kharkov 61108, Ukraine*
[32] *Randolph Macon College, Ashlan, Virginia 23005, USA*
[33] *Cairo University, Cairo 121613, Egypt*
[34] *Virginia Polytechnic Inst. & State Univ., Blacksburg, Virginia 234061, USA*
[35] *Stony Brook, State University of New York, New York 11794, USA*
[36] *Cornell University, Ithaca, New York 14853, USA*

[37] University of New Hampshire, Durham, New Hampshire 03824, USA
[38] Columbia University, New York, New York 10027, USA
[39] University of Manitoba, Winnipeg, MB R3T 2N2, Canada
[40] Rutgers University, New Brunswick, New Jersey 08854, USA
[41] Duke University, Durham, North Carolina 27708, USA
[42] Norfolk State University, Norfolk, Virginia 23504, USA
[43] Physics Division, Argonne National Laboratory, Lemont, IL 60439, USA
[44] Saint Mary's University, Halifax, Nova Scotia B3H 3C3, Canada
[45] Rensselaer Polytechnic Institute, Troy, NY 12180, USA
[46] Mississippi State University, Mississippi State, Mississippi 39762, USA
[47] AANL, 2 Alikhanian Brothers Street, 0036, Yerevan, Armenia
[48] Faculty of Mathematics and Physics, University of Ljubljana, 1000 Ljubljana, Slovenia
[49] Shandong University, Jinan, China
[50] Duquesne University, 600 Forbes Ave, Pittsburgh, Pennsylvania 15282, USA
[51] Huangshan University, Tunxi, Daizhen Rd, China
[52] University of Science and Technology of China, Hefei, Anhui 230026, China

(Dated: November 24, 2020)

We report measurements of the exclusive neutral pion electroproduction cross section off protons at large values of x_B (0.36, 0.48 and 0.60) and Q^2 (3.1 to 8.4 GeV^2) obtained from Jefferson Lab Hall A experiment E12-06-014. The corresponding structure functions $d\sigma_L/dt + \epsilon d\sigma_T/dt$, $d\sigma_{TT}/dt$, $d\sigma_{LT}/dt$ and $d\sigma_{LT'}/dt$ are extracted as a function of the proton momentum transfer $t - t_{min}$.

The results suggest the amplitude for transversely polarized virtual photons continues to dominate the cross section throughout this kinematic range. The data are well described by calculations based on transversity Generalized Parton Distributions coupled to a helicity flip Distribution Amplitude of the pion, thus providing a unique way to probe the structure of the nucleon.

Generalized Parton Distributions (GPDs) [1–3] describe the three-dimensional structure of the nucleon by correlating the transverse position and the longitudinal momentum of the quarks and gluons inside of it. GPDs are accessible through deep exclusive processes, such as Deeply Virtual Compton Scattering (DVCS) and Deeply Virtual Meson Production (DVMP). For the latter, collinear factorization theorems [4] applied to longitudinally polarized virtual photons only (not to the transversely polarized ones) establish that the DVMP amplitude factorizes into a hard perturbative part and a soft component described by the GPDs of the nucleon. Figure 1 shows the leading mechanism of the π^0 electroproduction reaction and defines the kinematic variables of the process. There are four chiral-even GPDs that conserve the quark helicity and four chiral-odd (transversity) GPDs that flip it. In the Bjorken limit where $Q^2 \to \infty$, the energy of the virtual photon $\nu \to \infty$ and $t/Q^2 \ll 1$, the reaction cross section is dominated by the contribution of longitudinally polarized virtual photons. This longitudinal component depends on the momentum transfer as Q^{-6}, whereas the transverse component goes as Q^{-8}. The longitudinal cross section of DVMP only depends on chiral-even GPDs of the nucleon. However, existing data [5–9] for neutral pseudoscalar meson production, with limited reach in Q^2 and in the quark valence regime show that transversely polarized virtual photons dominate the total cross section. In the collinear approximation, singularities occur for transversely polarized photons and mesons. To explain the large transverse contribution to the π^0 electroproduction cross sections, it has been suggested [10, 11] to regularize these singularities by including transverse degrees of freedom of the quarks and anti-quarks making up the meson. In this framework, the π^0 electroproduction cross section is described by the convolution of the Distribution Amplitudes (DA) of the meson and the transversity GPDs of the nucleon. Calculations based on this approach [10, 11] were able to reproduce reasonably well the existing neutral pseudoscalar meson production data cited above. This letter reports measurements of π^0 electroproduction cross sections that extend to higher than existing values of Q^2 (from 3.1 to 8.4 GeV^2) and of x_B (0.36, 0.48 and 0.60), with a large coverage in t and center of mass energy s.

The exclusive meson electroproduction cross section can be written as [12]:

$$\frac{d^4\sigma}{dQ^2 dx_B dt d\phi} = \frac{1}{2\pi}\frac{d^2\,\Gamma_\gamma}{dQ^2 dx_B}(Q^2, x_B, E) \left[\frac{d\sigma_{\rm T}}{dt} + \epsilon\frac{d\sigma_{\rm L}}{dt} + \sqrt{2\epsilon(1+\epsilon)}\frac{d\sigma_{\rm LT}}{dt}\cos(\phi) + \epsilon\frac{d\sigma_{\rm TT}}{dt}\cos(2\phi) + h\sqrt{2\epsilon(1-\epsilon)}\frac{d\sigma_{\rm LT'}}{dt}\sin(\phi)\right], \quad (1)$$

where $h(\pm 1)$ is the helicity of the initial lepton, E is the incident beam energy and ϕ is an angle between leptonic and hadronic planes defined according to the Trento convention [13]. The kinematic factor $\frac{d^2\,\Gamma_\gamma}{dQ^2 dx_B}$ and ϵ are the virtual photon flux and the degree of longitudinal polar-

* rochej@ohio.edu

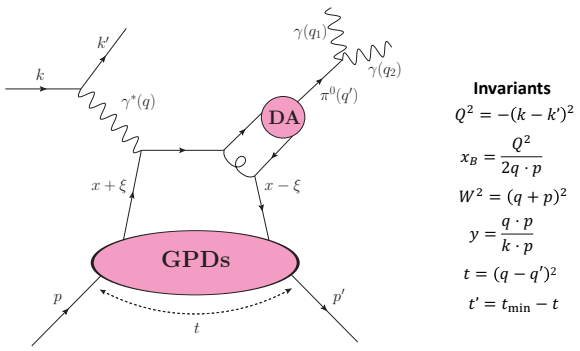

FIG. 1. Leading twist diagram representing the pseudoscalar DVMP to the $\gamma\gamma$ channel. The net four-momentum transferred to the proton is t, whose minimum value t_{min} occurs when the π^0 meson is emitted parallel to the virtual photon. The average light-cone momentum fraction carried by the struck parton is x with -2ξ the light-cone momentum transfer. The hadronization is described by meson Distribution Amplitudes (DA).

ization defined as:

$$\frac{d^2\,\Gamma_\gamma}{dQ^2 dx_B}(Q^2, x_B, E) = \frac{\alpha}{8\pi}\,\frac{1}{1-\epsilon}\,\frac{1-x_B}{x_B^3}\,\frac{Q^2}{M_p^2 E^2}\,, \quad (2)$$

where M_p is the proton mass and

$$\epsilon = \frac{1 - y - \frac{Q^2}{4E^2}}{1 - y + \frac{y^2}{2} + \frac{Q^2}{4E^2}} \quad (3)$$

with $y = [q \cdot p]/[k \cdot p]$.

Experiment E12-06-114 took data between 2014 and 2016 in Jefferson Lab Hall A. The main goal of this experiment was to measure the DVCS cross section $ep \to ep\gamma$. The same experimental configuration also captured exclusive π^0 production events. The kinematics covered by the experiment are shown in Tab. I. The electron beam scattered off a 15-cm-long liquid hydrogen target with luminosities greater than 10^{38} cm^{-2}s^{-1}. The beam polarization measured by the Hall A Møller polarimeter was $86 \pm 1\%$, with the uncertainty dominated by the systematic precision of the measurement. Scattered electrons were detected in a High-Resolution Spectrometer (HRS) with a relative momentum resolution of $2{\cdot}10^{-4}$ and a horizontal angular resolution of 2 mr [14]. Photons from the DVCS and DVMP processes were measured in an electromagnetic calorimeter consisting of a 13×16 array of PbF_2 crystals. The analog signal of each channel was sampled by a 1 GHz Analog Ring Sampler [15, 16] and recorded over 128 ns. The calorimeter was calibrated multiple times during the experiment using coincident elastic H(e, $e'_{\rm Calo}$ $p_{\rm HRS}$) events. The typical energy resolution of the calorimeter was 3% at 4.2 GeV with an angular resolution of 1.5 mr (when located 6 m from the target). Between two consecutive elastic calibrations, the output of the calorimeter for a given photon energy changed up to 10% due to the radiation damage of the PbF_2 crystals. The loss of signal was estimated and compensated for by adjusting the reconstructed invariant mass of the detected π^0 events.

Neutral pions were reconstructed by selecting 2 photons in the calorimeter above 500 MeV each, in coincidence with the detection of a scattered electron in the HRS. The HRS-calorimeter coincidence-time resolution was about 1 ns. The total contribution from accidental coincidences was below 2% and was subtracted from the experimental yield. The π^0 sample was cleanly identified by selecting events around the invariant mass $m_{\gamma\gamma} = \sqrt{(q_1 + q_2)^2}$. The exclusivity of the reaction was ensured by reconstructing the missing-mass squared M_X^2 of the $H(e, e'\gamma\gamma)X$ reaction (Fig. 2).

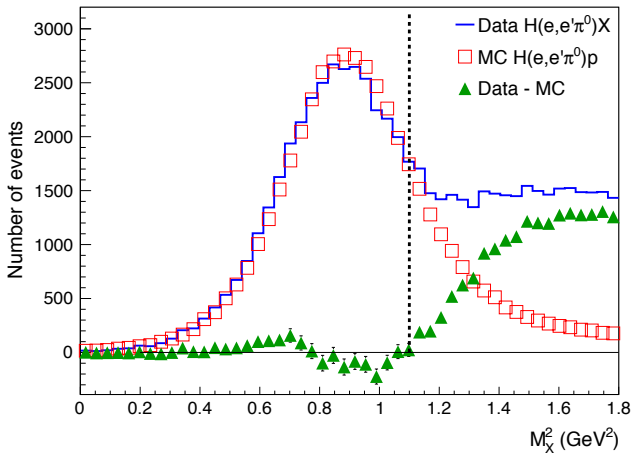

FIG. 2. Missing-mass squared for $H(e, e'\pi^0)X$ events. The deviation of the experimental yield from the exclusive π^0 simulated data show the contribution of inclusive channels above the additional pion production threshold at $(M_p + m_{\pi^0})^2 \approx 1.15$ GeV^2. The dotted line indicates the cut $M_X^2 < 1.1$ GeV^2 applied in order to remove this background. A cut on the invariant π^0 mass between 105 MeV and 165 MeV was also applied to ensure exclusivity.

The acceptance and resolution of the experiment were computed by a Monte-Carlo simulation based on the GEANT4 software [17]. The simulation and cross section extraction includes the real and virtual radiative effects, based on calculations by Vanderhaeghen *et al.* [18].

During most of the experiment, the first quadrupole of the HRS was not fully functional and had to be operated at a reduced current. Effects on the spectrometer acceptance were taken into account for each kinematic setting and period by applying the same multi-dimensional cut [19] to both the experimental and simulated data.

Data were binned into 12 ϕ bins by 5 t' bins. The different structure functions appearing in the π^0 electroproduction cross section were extracted by exploiting their specific ϕ dependencies, minimizing the χ^2 between the

x_B-label	0.36			0.48				0.60	
$\langle x_B \rangle$	0.36	0.36	0.36	0.48	0.45	0.46	0.46	0.59	0.60
E (GeV)	7.38	8.52	10.59	4.49	8.85	8.85	10.99	8.52	10.59
Q^2 (GeV^2)	3.11	3.57	4.44	2.67	4.06	5.16	6.56	5.49	8.31
W^2 (GeV^2)	6.51	7.29	8.79	3.81	5.62	6.67	8.32	4.58	6.46
$-t_{min}$ (GeV^2)	0.16	0.17	0.17	0.33	0.35	0.35	0.36	0.67	0.71
ϵ	0.61	0.62	0.63	0.51	0.71	0.55	0.52	0.66	0.50

TABLE I. Incident beam energy E and average values for scattering kinematic variables for each of the nine (E, Q^2, x_B) settings where the π^0 cross sections are reported. For each setting, cross sections are measured as a function of $t' = t_{min} - t$, with t_{min} calculated event-by-event.

number of experimental and simulated events:

$$\chi^2 = \sum_{i=1}^{\mathcal{N}=60} \left(\frac{N_i^{exp} - N_i^{sim}}{\sigma_i^{exp}} \right)^2 \qquad (4)$$

where the sum runs over all 12×5 bins for each (x_B, Q^2) setting. N_i^{exp} is the total number of events in bin i with corresponding statistical precision σ_i^{exp}. The number of simulated events in bin i is computed by convoluting the acceptance and resolution of the experimental setup with the kinematic dependencies of each of the structure functions ($d\sigma_L/dt + \epsilon d\sigma_T/dt$, $d\sigma_{TT}/dt$, $d\sigma_{LT}/dt$ and $d\sigma_{LT'}/dt$) that make up the cross section (see Eq. 1). These structure functions are the free parameters of the χ^2 minimization. Bin migration effects from one kinematic bin to another due to resolution and radiative effects are incorporated into the simulation and are up to 10% depending upon the kinematic bin. Cross sections are only reported for the 4 lowest t' bins; the additional highest t' bin in the analysis is only used to evaluate bin migration to the lower t' bins. The systematic uncertainty associated with the bin migration is assessed by varying the selection cut on the missing mass-squared, for each kinematic bin. Figure 3 shows the four structure functions and their ϕ dependence measured at one of the settings. The helicity-dependent structure function $d\sigma_{LT'}$ is extracted by a similar fit to the difference in yield for events with opposite helicities.

For all kinematic settings, inclusive Deeply Inelastic Scattering (DIS) data were taken simultaneously with the main DVCS/π^0 sample by using an ancillary prescaled trigger. These ancillary measurements allowed to benchmark this data taking and analysis against well known absolute cross sections. The DIS cross sections extracted from these ancillary data were 4% lower on average than the empirical fit described in Ref. [20]. This systematic deviation of the DIS data from the reference is believed to arise from the time slewing of the signal from a large HRS scintillator paddle (S0), which was used in the ancillary DIS trigger but not in the main HRS-calorimeter coincidence trigger. Furthermore, the DIS cross sections extracted from these ancillary data had a $\pm 4\%$ spread among the different kinematics settings. The estimated individual systematic uncertainties associated with luminosity, electron tracking efficiency, HRS acceptance, and acquisition deadtime added in quadrature to 3.5%. The reported precision of the model in [20] against which these measurements are compared is 2%. Both these sources of uncertainty can explain the 4% spread obtained in the comparison. The total systematic uncertainty of the π^0 electroproduction cross section measurements includes the uncertainty on the electron detection and acceptance, the luminosity evaluation, and the uncertainty on the photon detection and the exclusivity selection criteria. The latter was estimated by studying the variation of the results as a function of the M_X^2 and calorimeter energy threshold cuts. The total systematic uncertainty of the results reported herein varies between 4% and 8% depending on the kinematic setting.

Figure 4 shows the measurements of the different structure functions at the kinematics settings detailed in Tab. I. The asymptotic behavior of the $\phi-$independent

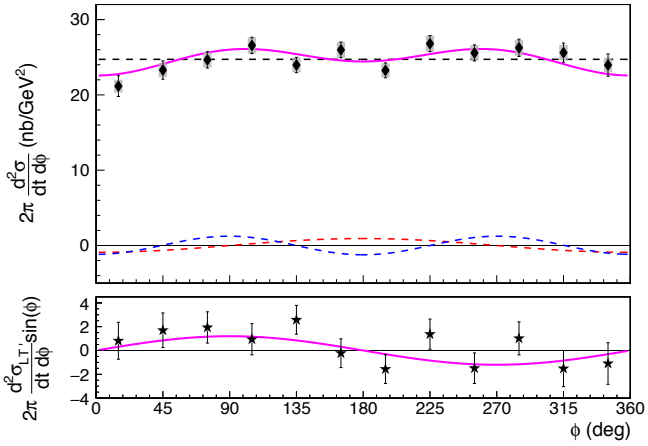

FIG. 3. Helicity-independent (top) and helicity-dependent (bottom) cross sections (black points) at Q^2= 8.31 GeV^2, $t' = 0.15$ GeV^2, and x_B=0.60. Bars around the points show statistical uncertainties. The gray boxes that surround the data represent the systematic uncertainties. The solid curves show the fit to the total helicity-independent and helicity-dependent cross sections and dashed curves show the contributions rising from each of the individual structure functions of Eq. 1 : $d\sigma_U = d\sigma_T + \epsilon d\sigma_L$ (black), $d\sigma_{TT}$ (blue) and $d\sigma_{LT}$ (red).

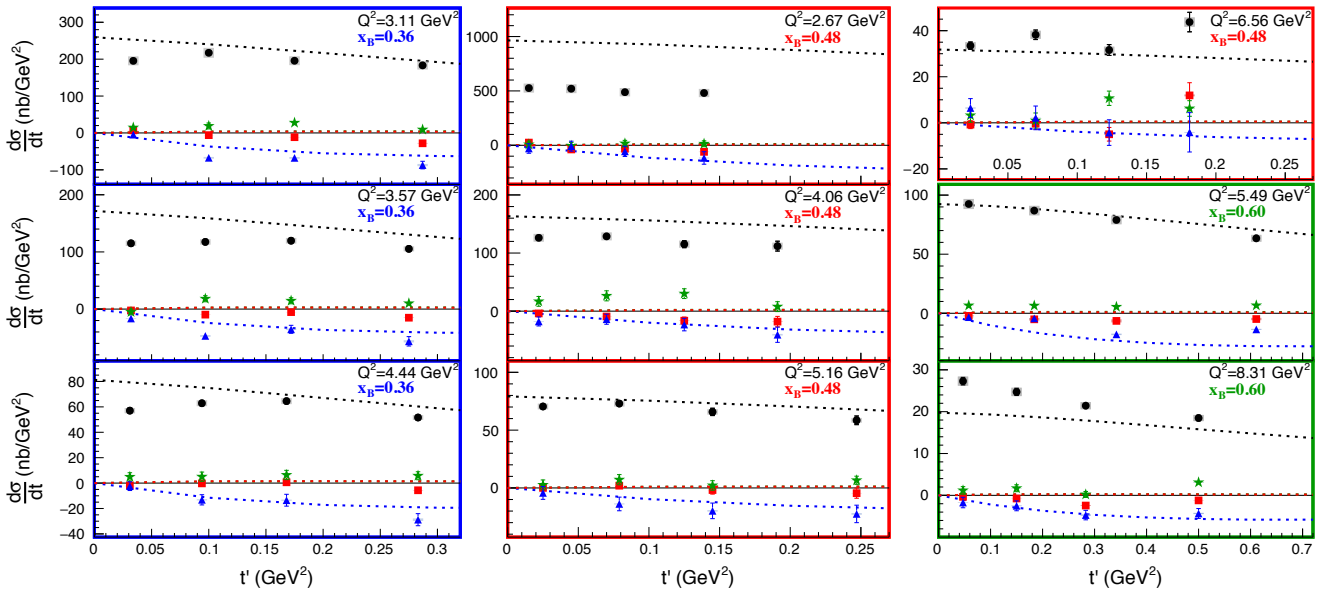

FIG. 4. Differential cross sections for all kinematic settings as a function of $t' = t_{min} - t$: $d\sigma_U = d\sigma_T + \epsilon d\sigma_L$ (black circles), $d\sigma_{LT}$ (red squares), $d\sigma_{TT}$ (blue triangles), and $d\sigma_{LT'}$ (green stars). The dashed curves are calculations based on transversity GPDs of the nucleon [11]; at this scale the predictions for the $d\sigma_{LT}$ and the $d\sigma_{LT'}$ overlay each other. The uncertainty bars are statistical only. The gray box surrounding the data points show the systematic uncertainty. The panels with the same x_B value share a common t' scale, which nonetheless varies with x_B.

contribution $d\sigma_U = d\sigma_T + \epsilon\sigma_L$ at high Q^2 is expected to be dominated by $d\sigma_L$. However, calculations of this structure function based on chiral-even GPD parametrizations that reproduce worldwide DVCS data failed drastically to reproduce this value at moderate Q^2 [7]. The modified factorization approach first introduced in [10, 11] provides a large contribution to the transverse amplitude of π^0 electroproduction, which arises from the convolution of the chiral-odd (transversity) GPDs of the nucleon with a quark-helicity flip pion DA. At moderate Q^2 (less than 3 GeV^2), these calculations show a reasonably good agreement between the $d\sigma_U$ they computed and the data [7]. At the larger Q^2 range presented here (3 to 8.5 GeV^2), the $d\sigma_U$ computed by these models is still in reasonable (as within an order of magnitude) agreement with the data as depicted in Fig. 4. The transverse-transverse interference structure function $d\sigma_{TT}$ is also well described by these calculations. This overall successful description of the data supports the exciting possibility to probe the transversity GPDs of the nucleon through neutral pion electroproduction.

The data set presented herein expands significantly the kinematics of exclusive neutral pion production cross section measurements, with a large Q^2 and x_B range. In particular, these data will constrain the parameters controlling the x-dependence of the tranversity GPDs H_T and $\widetilde{E}_T$ in future global fits.

Finally, these data also reach large values of $t = t_{min} - t'$, with the central value of $-t$ up to 1.3 GeV^2. The $t-$dependence of the cross section, usually parametrized by Regge-like profile functions, is no longer valid at typical values of $-t > 1$ GeV^2. This was realized in the GPD analysis of nucleon form factors [21]. The theory calculations shown in Fig. 4 include a profile function with a strong $x-t$ correlation [22], which also allows the proton radius to remain finite as $x \to 1$ and allows the proton form factors—the lowest moments of GPDs–to behave as powers of t at large $-t$.

The calculations for $d\sigma_{LT}$ and $d\sigma_{LT'}$ underestimate the data in most of the kinematic settings. This hints at a larger contribution of the longitudinal amplitude than the one expected in the modified factorization approach. However, one must point out that these calculations are obtained using some kinematic approximations, such as $\xi \approx x_B/(2 - x_B)$. Recent theory developments [23] have shown that power corrections of $\mathcal{O}(t/Q^2)$ and $\mathcal{O}(M_p/Q^2)$ should be included and recent DVCS data [24] at similar kinematics have been proved sensitive to these effects.

The Q^2-dependence of $d\sigma_U$ is shown in Fig. 5 at three values of x_B at constant $t' = 0.1$ GeV^2. At sufficiently high Q^2, it is expected that $d\sigma_L \sim Q^{-6}$ and $d\sigma_T \sim Q^{-8}$. While our results seem to be dominated by the $d\sigma_T$ contribution, the Q^2-dependence of $d\sigma_U$ is closer to Q^{-6} than Q^{-8}. This confirms the fact that at these values of Q^2 and x_B the asymptotic limit is still far away. The Q^2-dependence observed is slightly flatter than the one from the GK calculations [11], which is closer to $\sim Q^{-8}$. This also supports the fact that a non-negligible longitudinal amplitude is needed to describe the data at these kinematics. A broader perspective on the Q^2- and t-dependence of these results is presented in Tab. II. At each x_B setting, we fit the data to a func-

tional form $C(Q^2)^A \exp(-Bt')$. These fits reiterate the approximately global $1/Q^6$ behavior of the cross section over the t' and x_B range.

An L/T separation of the π^0 electroproduction cross section at these high values of x_B will provide a definite answer on the size of the longitudinal contribution. This is the goal of an upcoming experiment [25] in Hall C at Jefferson Lab which is expected to run within the next 2 years.

TABLE II. Combined (Q^2, t') fits $d\sigma_U = C(Q^2)^A \exp(-Bt')$at each x_B setting. Only the data of this publication are included. The fits and error bars are based on the statistical and systematic uncertainties of the data, added in quadrature.

x_B	C	A	B	χ^2	№
	μb/GeV^2		GeV^{-2}	Total	d.o.f.
0.36	8.6 ± 1.4	3.3 ± 0.1	0.34 ± 0.17	18.	9
0.48	8.3 ± 0.9	2.9 ± 0.1	0.69 ± 0.3	27.	13
0.60	$20. \pm 4.$	3.1 ± 0.1	0.75 ± 0.1	1.6	5

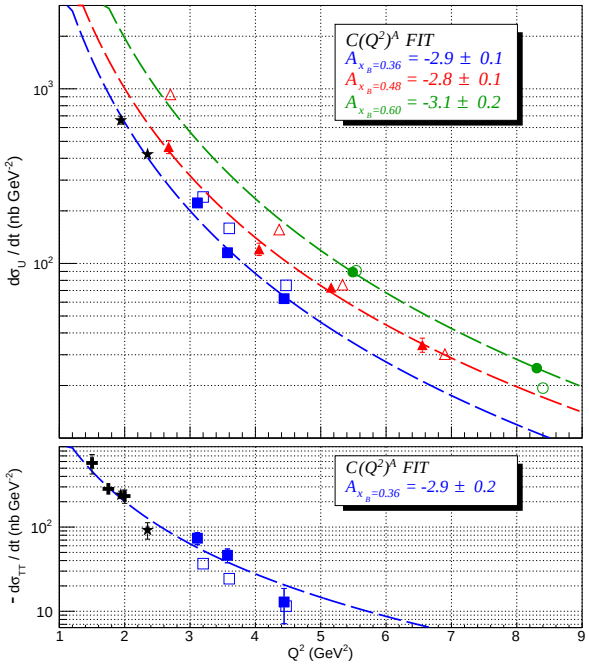

FIG. 5. The Q^2 dependence of the structure functions $d\sigma_U$ and $-d\sigma_{TT}$ at average $t' = 0.1$ GeV^2. The solid markers are the experimental results, and the open markers are the GK model predictions. The $d\sigma_U$ amd $-d\sigma_{TT}$ from this experiment and the fitted functions at the settings $x_B = 0.36$, 0.48, and 0.60 are shown in blue, red, and green respectively. The black stars and crosses show the results from [5] and [7] correspondingly, which are also included in the fit at $x_B = 0.36$.

ACKNOWLEDGEMENTS

We thank P. Kroll for very fruitful discussions about these results. We acknowledge essential contributions by the Hall A collaboration and Accelerator and Physics Division staff at Jefferson Lab. This material is based upon work supported by the U.S. Department of Energy, Office of Science, Office of Nuclear Physics under contract DE-AC05-06OR23177. This work was also supported a DOE Early Career Award to S. Covrig Dusa for the development of the high power hydrogen target cells, the National Science Foundation (NSF), the French CNRS/IN2P3, ANR, and P2IO Laboratory of Excellence, and the Natural Sciences and Engineering Research Council of Canada (NSERC).

[1] X. Ji, Gauge invariant decomposition of nucleon spin, Phys. Rev. Lett. **78**, 610 (1997).

[2] D. Müller, D. Robaschik, B. Geyer, F. M. Dittes, and J. Horejsi, Wave functions, evolution equations and evolution kernels from light-ray operators of QCD, Fortschr. Phys. **42**, 101 (1994).

[3] A. V. Radyushkin, Nonforward parton distributions, Phys. Rev. **D56**, 5524 (1997).

[4] J. C. Collins, L. Frankfurt, and M. Strikman, Factorization for hard exclusive electroproduction of mesons in QCD, Phys. Rev. **D56**, 2982 (1997).

[5] E. Fuchey *et al.*, Exclusive Neutral Pion Electroproduction in the Deeply Virtual Regime, Phys. Rev. C **83**, 025201 (2011).

[6] I. Bedlinskiy *et al.* (CLAS), Measurement of Exclusive π^0 Electroproduction Structure Functions and their Relationship to Transversity GPDs, Phys. Rev. Lett. **109**, 112001 (2012).

[7] M. Defurne *et al.* (Jefferson Lab Hall A Collaboration), Rosenbluth separation of the π^0 electroproduction cross section, Phys. Rev. Lett. **117**, 262001 (2016).

[8] M. Mazouz *et al.* (Jefferson Lab Hall A), Rosenbluth separation of the π^0 Electroproduction Cross Section off the Neutron, Phys. Rev. Lett. **118**, 222002 (2017).

[9] M. Alexeev *et al.* (COMPASS), Measurement of the cross section for hard exclusive π^0 muoproduction on the proton, Phys. Lett. B **805**, 135454 (2020).

[10] S. Ahmad, G. R. Goldstein, and S. Liuti, Nucleon tensor charge from exclusive π^0 electroproduction, Phys. Rev. D **79**, 054014 (2009).

[11] S. V. Goloskokov and P. Kroll, Transversity in hard exclusive electroproduction of pseudoscalar mesons, Eur. Phys. J. **A47**, 112 (2011).

[12] D. Drechsel and L. Tiator, Threshold pion photoproduction on nucleons, J. Phys. G **18**, 449 (1992).

[13] A. Bacchetta, U. D'Alesio, M. Diehl, and C. A. Miller, Single-spin asymmetries: The trento conventions, Phys. Rev. **D70**, 117504 (2004).

[14] J. Alcorn *et al.*, Basic Instrumentation for Hall A at Jefferson Lab, Nucl. Instrum. Meth. **A522**, 294 (2004).

[15] F. Feinstein (ANTARES), The analogue ring sampler: A front-end chip for ANTARES, Nucl. Instrum. Meth. **A504**, 258 (2003).

[16] F. Druillole, D. Lachartre, F. Feinstein, E. Delagnes, H. Lafoux, C. Hadamache, and J. Fopma (ANTARES), The analog ring sampler: An ASIC for the front-end electronics of the ANTARES neutrino telescope, *Nuclear science. Proceedings, Symposium, NSS 2001, San Diego, USA, November 4-10, 2001*, IEEE Trans. Nucl. Sci. **49**, 1122 (2002).

[17] S. Agostinelli and others (GEANT4 collaboration), GEANT4: A Simulation toolkit, Nucl. Instrum. Meth. A **506**, 250 (2003).

[18] M. Vanderhaeghen, J. M. Friedrich, D. Lhuillier, D. Marchand, L. Van Hoorebeke, and J. Van de Wiele, QED radiative corrections to virtual Compton scattering, Phys. Rev. **C62**, 025501 (2000).

[19] M. Rvachev, *Effective Use of Hall A Spectrometer with R-Function*, (Jefferson Lab, 2001).

[20] M. E. Christy and P. E. Bosted, Empirical fit to precision inclusive electron-proton cross- sections in the resonance region, Phys. Rev. **C81**, 055213 (2010).

[21] M. Diehl and P. Kroll, Nucleon form factors, generalized parton distributions and quark angular momentum, Eur. Phys. J. C **73**, 2397 (2013).

[22] P. Kroll, The GPD $\tilde{H}$ and spin correlations in wide-angle Compton scattering, Eur. Phys. J. A **53**, 130 (2017).

[23] V. M. Braun, A. N. Manashov, D. Müller, and B. M. Pirnay, Deeply virtual compton scattering to the twist-four accuracy: Impact of finite-t and target mass corrections, Phys. Rev **D89**, 074022 (2014).

[24] M. Defurne *et al.*, A glimpse of gluons through deeply virtual compton scattering on the proton, Nature Commun. **8**, 1408 (2017).

[25] Hyde, C.E., Muñoz Camacho, C., Roche, J. and others, *Exclusive Deeply Virtual Compton and Neutral Pion Cross-Section Measurements in Hall C*, Proposal E12-13-010 (Jefferson Lab, 2013) https://www.jlab.org/exp_prog/proposals/13/PR12-13-010.pdf.

	$[t'_{low}, t'_{up}]$	$\langle t' \rangle$ (GeV^2)	σ_U (nb/GeV^2)	σ_{LT} (nb/GeV^2)	σ_{TT} (nb/GeV^2)	$\sigma_{LT'}$ (nb/GeV^2)
$x_B = 0.36$	[0.00, 0.07]	0.03	195.46 ± 3.66 ± 11.93	7.05 ± 3.19 ± 0.25	-4.66 ± 7.62 ± 0.16	14.52 ± 6.91 ± 0.51
$Q^2 = 3.11$	[0.07, 0.13]	0.10	217.29 ± 4.22 ± 13.26	-5.97 ± 3.81 ± 0.21	-67.45 ± 9.03 ± 2.36	18.91 ± 8.05 ± 0.66
	[0.13, 0.22]	0.18	195.76 ± 4.15 ± 11.95	-11.55 ± 4.01 ± 0.40	-67.67 ± 8.97 ± 2.37	27.63 ± 7.17 ± 0.97
	[0.22, 0.38]	0.29	183.18 ± 4.54 ± 11.18	-28.08 ± 4.63 ± 0.98	-87.12 ± 10.23 ± 3.05	9.05 ± 6.38 ± 0.32
$x_B = 0.36$	[0.00, 0.06]	0.03	115.04 ± 2.53 ± 4.64	-2.37 ± 2.18 ± 0.08	-16.48 ± 5.25 ± 0.58	-5.08 ± 4.97 ± 0.18
$Q^2 = 3.57$	[0.06, 0.13]	0.10	117.51 ± 2.77 ± 4.74	-9.70 ± 2.54 ± 0.34	-46.96 ± 5.85 ± 1.64	18.11 ± 5.31 ± 0.63
	[0.13, 0.22]	0.17	119.61 ± 3.35 ± 4.82	-5.32 ± 3.52 ± 0.19	-35.39 ± 6.99 ± 1.24	14.58 ± 5.31 ± 0.51
	[0.22, 0.35]	0.28	105.37 ± 4.06 ± 4.25	-15.08 ± 4.61 ± 0.53	-56.36 ± 8.24 ± 1.97	10.04 ± 4.88 ± 0.35
$x_B = 0.36$	[0.00, 0.06]	0.03	57.04 ± 1.88 ± 2.08	-1.84 ± 1.44 ± 0.06	-2.42 ± 3.43 ± 0.08	4.92 ± 3.24 ± 0.17
$Q^2 = 4.44$	[0.06, 0.13]	0.09	62.86 ± 2.16 ± 2.29	-0.23 ± 1.83 ± 0.01	-13.17 ± 4.03 ± 0.46	5.04 ± 3.63 ± 0.18
	[0.13, 0.21]	0.17	64.53 ± 2.47 ± 2.35	0.62 ± 2.35 ± 0.02	-13.49 ± 4.66 ± 0.47	6.39 ± 3.65 ± 0.22
	[0.21, 0.38]	0.28	51.63 ± 2.56 ± 1.88	-5.66 ± 2.61 ± 0.20	-28.80 ± 4.76 ± 1.01	5.79 ± 3.13 ± 0.20
$x_B = 0.48$	[0.00, 0.03]	0.01	525.95 ± 14.48 ± 41.16	25.07 ± 16.53 ± 0.88	-29.14 ± 43.88 ± 1.02	7.60 ± 30.21 ± 0.27
$Q^2 = 2.67$	[0.03, 0.06]	0.04	520.40 ± 16.36 ± 40.73	-38.25 ± 19.21 ± 1.34	-7.88 ± 45.79 ± 0.28	-5.32 ± 31.83 ± 0.19
	[0.06, 0.11]	0.08	488.33 ± 17.33 ± 38.22	-31.60 ± 21.71 ± 1.11	-55.44 ± 47.02 ± 1.94	16.70 ± 28.69 ± 0.5
	[0.11, 0.18]	0.14	480.77 ± 23.45 ± 37.63	-60.20 ± 30.66 ± 2.11	-116.12 ± 57.67 ± 4.06	14.05 ± 27.05 ± 0.49
$x_B = 0.48$	[0.00, 0.05]	0.02	126.23 ± 3.84 ± 6.71	-3.93 ± 3.36 ± 0.14	-17.69 ± 7.80 ± 0.62	16.81 ± 8.43 ± 0.59
$Q^2 = 4.06$	[0.05, 0.10]	0.07	128.70 ± 4.65 ± 6.84	-9.18 ± 4.45 ± 0.32	-13.90 ± 8.66 ± 0.49	26.38 ± 8.65 ± 0.92
	[0.10, 0.16]	0.12	115.22 ± 6.01 ± 6.12	-16.42 ± 6.24 ± 0.57	-23.10 ± 10.78 ± 0.81	30.12 ± 8.41 ± 1.05
	[0.16, 0.23]	0.19	111.89 ± 8.46 ± 5.95	-18.01 ± 8.97 ± 0.63	-40.59 ± 13.09 ± 1.42	7.79 ± 8.51 ± 0.27
$x_B = 0.48$	[0.00, 0.05]	0.03	70.45 ± 2.53 ± 2.47	0.04 ± 2.23 ± 0.00	-4.31 ± 5.55 ± 0.15	2.63 ± 4.28 ± 0.09
$Q^2 = 5.16$	[0.05, 0.11]	0.08	72.98 ± 2.78 ± 2.55	1.96 ± 2.64 ± 0.07	-13.84 ± 5.89 ± 0.46	7.15 ± 4.40 ± 0.25
	[0.11, 0.19]	0.14	65.77 ± 3.17 ± 2.30	-1.82 ± 3.51 ± 0.06	-19.81 ± 6.74 ± 0.69	2.16 ± 4.12 ± 0.08
	[0.19, 0.33]	0.25	58.49 ± 3.74 ± 2.05	-4.52 ± 4.40 ± 0.16	-22.46 ± 7.55 ± 0.79	6.62 ± 3.53 ± 0.23
$x_B = 0.48$	[0.00, 0.05]	0.02	33.48 ± 1.60 ± 1.54	-0.79 ± 1.73 ± 0.03	6.43 ± 4.08 ± 0.23	3.23 ± 2.96 ± 0.11
$Q^2 = 6.56$	[0.05, 0.10]	0.07	38.21 ± 2.06 ± 1.76	-0.39 ± 2.39 ± 0.01	2.15 ± 5.14 ± 0.08	0.98 ± 3.30 ± 0.03
	[0.10, 0.15]	0.12	31.61 ± 2.35 ± 1.46	-4.97 ± 2.95 ± 0.17	-4.24 ± 5.56 ± 0.15	10.66 ± 3.11 ± 0.37
	[0.15, 0.21]	0.18	43.74 ± 4.23 ± 2.02	11.91 ± 5.51 ± 0.42	-4.12 ± 8.54 ± 0.14	6.22 ± 3.39 ± 0.22
$x_B = 0.60$	[0.00, 0.12]	0.06	92.48 ± 1.42 ± 4.26	-2.18 ± 0.70 ± 0.44	-3.29 ± 1.67 ± 0.12	6.61 ± 1.68 ± 0.23
$Q^2 = 5.49$	[0.12, 0.26]	0.18	86.89 ± 1.39 ± 4.01	-5.12 ± 0.75 ± 1.04	-4.28 ± 1.66 ± 0.15	6.47 ± 1.60 ± 0.23
	[0.26, 0.44]	0.34	78.96 ± 1.38 ± 3.64	-6.44 ± 0.86 ± 1.31	-17.84 ± 1.74 ± 0.62	5.47 ± 1.47 ± 0.19
	[0.44, 0.88]	0.61	63.43 ± 1.37 ± 2.92	-4.87 ± 1.03 ± 0.99	-13.65 ± 1.82 ± 0.48	6.66 ± 1.10 ± 0.23
$x_B = 0.60$	[0.00, 0.09]	0.05	27.29 ± 0.90 ± 1.10	-0.36 ± 0.48 ± 0.01	-1.72 ± 1.25 ± 0.06	1.18 ± 0.90 ± 0.04
$Q^2 = 8.31$	[0.09, 0.21]	0.15	24.72 ± 0.86 ± 1.00	-0.75 ± 0.48 ± 0.03	-2.50 ± 1.18 ± 0.09	1.70 ± 0.83 ± 0.06
	[0.21, 0.36]	0.28	21.43 ± 0.81 ± 0.86	-2.43 ± 0.49 ± 0.09	-4.71 ± 1.13 ± 0.16	0.21 ± 0.71 ± 0.01
	[0.36, 0.69]	0.50	18.48 ± 0.79 ± 0.74	-1.20 ± 0.58 ± 0.04	-4.33 ± 1.18 ± 0.15	3.10 ± 0.56 ± 0.11

TABLE III. Numerical values of the structure functions shown in Fig. 5. The first and second uncertainty values indicate the statistical and systematic uncertainties, respectively. $\langle t' \rangle$ is weighted average of events for each t' bin, with upper and lower bounds given by $[t'_{low}, t'_{up}]$.